

Exceptional Microscale Plasticity in Amorphous Aluminum Oxide at Room Temperature

Erkka J. Frankberg,* Aloshious Lambai, Jiahui Zhang, Janne Kalikka, Sergei Khakalo, Boris Paladino, Mattia Cabrioli, Nidhin G. Mathews, Turkka Salminen, Mikko Hokka, Jaakko Akola, Antti Kuronen, Erkki Levänen, Fabio Di Fonzo, and Gaurav Mohanty

Oxide glasses are an elementary group of materials in modern society, but brittleness limits their wider usability at room temperature. As an exception to the rule, amorphous aluminum oxide ($\alpha\text{-Al}_2\text{O}_3$) is a rare diatomic glassy material exhibiting significant nanoscale plasticity at room temperature. Here, it is shown experimentally that the room temperature plasticity of $\alpha\text{-Al}_2\text{O}_3$ extends to the microscale and high strain rates using in situ micropillar compression. All tested $\alpha\text{-Al}_2\text{O}_3$ micropillars deform without fracture at up to 50% strain via a combined mechanism of viscous creep and shear band slip propagation. Large-scale molecular dynamics simulations align with the main experimental observations and verify the plasticity mechanism at the atomic scale. The experimental strain rates reach magnitudes typical for impact loading scenarios, such as hammer forging, with strain rates up to the order of $1\,000\text{ s}^{-1}$, and the total $\alpha\text{-Al}_2\text{O}_3$ sample volume exhibiting significant low-temperature plasticity without fracture is expanded by 5 orders of magnitude from previous observations. The discovery is consistent with the theoretical prediction that the plasticity observed in $\alpha\text{-Al}_2\text{O}_3$ can extend to macroscopic bulk scale and suggests that amorphous oxides show significant potential to be used as light, high-strength, and damage-tolerant engineering materials.


1. Introduction

There are innumerable engineering applications for ductile materials that are stronger and lighter than current engineering materials, such as aluminum alloys and steels. Even though oxide glasses show a remarkable theoretical strength-to-density ratio, their low fracture resistance under unconfined loading (e.g., bending or pulling) is a major limitation, averting their use in large number of engineering applications where the possibility of a catastrophic brittle failure needs to be avoided at all costs. Oxide glasses are typically brittle at room temperature due to the absence of active plasticity mechanisms. Without plasticity, the applied elastic stress concentrates on the processing-induced flaws in the material, and, at a critical load, leads to an abrupt brittle failure.^[1] This has led to the current design paradigm in which glass and ceramic materials are typically considered as noncritical load-bearing components whose

E. J. Frankberg, A. Lambai, J. Zhang, N. G. Mathews, M. Hokka, E. Levänen, G. Mohanty
Materials Science and Environmental Engineering Unit
Tampere University
Korkeakoulunkatu 6, Tampere 33720, Finland
E-mail: erkka.frankberg@tuni.fi

E. J. Frankberg, B. Paladino, M. Cabrioli, F. Di Fonzo
Center for Nano Science and Technology CNST@Polimi
Istituto Italiano di Tecnologia
Via Pascoli 70/3, Milano 20133, Italy

J. Zhang, A. Kuronen
Department of Physics
University of Helsinki
P.O. Box 43, Helsinki FI-00014, Finland

 The ORCID identification number(s) for the author(s) of this article can be found under <https://doi.org/10.1002/adma.202303142>

© 2023 The Authors. Advanced Materials published by Wiley-VCH GmbH. This is an open access article under the terms of the Creative Commons Attribution License, which permits use, distribution and reproduction in any medium, provided the original work is properly cited.

DOI: 10.1002/adma.202303142

J. Kalikka, J. Akola
Computational Physics Laboratory
Tampere University
Korkeakoulunkatu 6, Tampere 33720, Finland

S. Khakalo
Integrated Computational Materials Engineering
VTT Technical Research Centre of Finland Ltd.
Vuorimiehentie 2, Espoo 02044, Finland

S. Khakalo
Department of Civil Engineering
Aalto University
Rakentajanaukio 4, Espoo 02150, Finland

T. Salminen
Tampere Microscopy Center
Tampere University
Korkeakoulunkatu 6, Tampere 33720, Finland

J. Akola
Department of Physics
Norwegian University of Science and Technology (NTNU)
Høgskoleringen 5, Trondheim NO-7491, Norway

main task is to offer other additional functionality to the application or device in question. For example, inorganic amorphous oxides show great promise for modern electronics, where they allow for a wide range of tailored, functional properties, from full dielectrics to tuned semiconductors coupled with visible light transparency, and they offer good chemical and thermal stability.^[2,3,4,5,6,7,8] However, in more realistic, unconfined impact-loading scenarios – such as a mobile device dropping on a hard floor ($1\text{--}10\text{ s}^{-1}$),^[9] or hammer forging ($10\text{--}100\text{ s}^{-1}$),^[10] or at the extreme, a full-frontal vehicle crash ($100\text{--}1000\text{ s}^{-1}$),^[11] – these materials cannot be used to bear load without the probable risk of a catastrophic failure.

Recently, Frankberg et al. discovered that thin films of amorphous aluminum oxide ($\text{a-Al}_2\text{O}_3$) exhibit significant unconfined plasticity at room temperature under all principal loading modes: shear, tension, and compression.^[12] Further atomistic simulations have confirmed the large potential for nanoscale plasticity in $\text{a-Al}_2\text{O}_3$.^[13,14] Frankberg et al. proposed that, theoretically, the observed viscous creep plasticity could extend up to bulk scale if the material is dense and flaw-free.^[12] In practice, to suppress crack nucleation and propagation, and to instead allow bulk plasticity, the glassy oxide material should be sufficiently free of both intrinsic flaws in the atomic structure and extrinsic processing flaws. To explore whether such flaw-free bulk glass structures can be fabricated, and whether these samples still exhibit similar plasticity at room temperature, one of the primary tasks for follow-up studies is to increase the experimental sample volume to the microscale and beyond. In the case of $\text{a-Al}_2\text{O}_3$, it is not trivial to produce larger samples, as it is a poor glass former and requires, for example, an ultra-high quench rate or a low processing temperature to retain an amorphous structure. In addition, the synthesis of dense and flaw-free $\text{a-Al}_2\text{O}_3$ requires a careful control of the process parameters.^[15,16] For clarity, non-crystalline materials produced using physical vapor deposition, such as pulsed laser deposition (PLD), are typically defined as “amorphous” materials, instead of “glass”, and therefore we define our experimental material as amorphous alumina.

Micropillar compression can be used to study low-temperature plasticity phenomena in ceramic and glass materials,^[17] which on the macroscopic scale normally exhibit fully brittle behavior under elastic loading. Typically, a limited plastic strain can be measured in the micropillars, which is accompanied by crack nucleation and propagation eventually leading to fracture.^[18,19] As an example, single crystalline sapphire ($\alpha\text{-Al}_2\text{O}_3$) micropillars compressed at room temperature show limited plasticity by dislocation slip, accompanied by local cracking and eventually fracture.^[20] In addition to the distinct brittle-to-ductile transition, it is known that limiting the ceramic or glass sample size to a micropillar, with both the diameter and height measured in micrometers, induces also other size-related effects, and can, for example, influence the observed yield stress of the material and the observed plastic strain prior to failure.^[21] In addition to size,

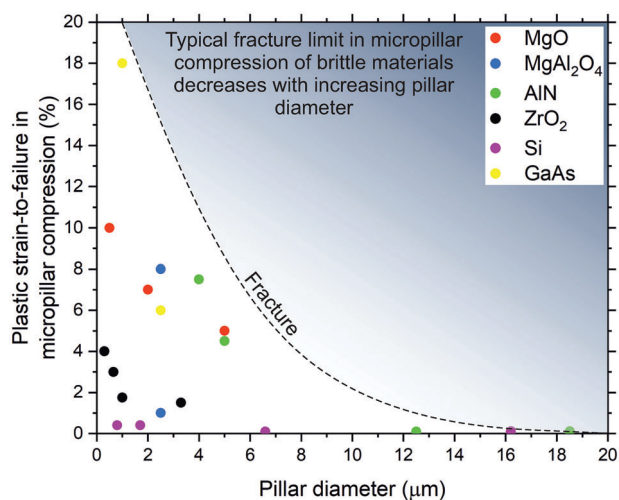


Figure 1. Reported plastic strain-to-failure in micropillar compression of crystalline ceramic and semiconductor materials at room temperature. Micropillar data on crystalline ceramics: single crystal (sc) MgO,^[24] sc AlN,^[25] polycrystalline ZrO₂,^[26] sc MgAl₂O₄,^[30] and semiconductors: sc Si,^[27] sc GaAs.^[28,29] The dashed line represents a trend of decreasing plasticity as a function of the micropillar diameter.

varying the strain rate in micropillar compression can also substantially alter the stress-strain response and induce a brittle-to-ductile transition.^[22] Further, fabricating micropillar samples using the focused ion beam technique can substantially affect the observed mechanical properties, and minimal ion exposure on the micropillars and caution in the following mechanical test result analysis are advised.^[23] Our survey on recent micropillar compression studies at room temperature indicates that the amount of plastic strain-to-failure reached in brittle ceramic and semiconductor materials is typically below 10%, and, as a trend, it decreases towards zero when increasing the pillar diameter towards bulkier samples (**Figure 1**).^[24,25,26,27,28,29,30] In addition, the experiments in the available literature are often performed at quasi-static strain rates ($< 10^{-1}\text{ s}^{-1}$), which are not relevant for most engineering applications.

Amorphous oxide micropillars deviate from this typical behavior and have already been shown to exhibit more significant plastic strain prior to failure under microcompression.^[22,31,32] Amorphous silica (a-SiO_2) micropillars with a 3.1 μm diameter and 4.75 μm height can be deformed plastically at up to 25% total strain at a quasi-static strain rate of 10^{-3} s^{-1} ; however, the straining induces vertical cracking of the pillars and fracture can occur during unloading.^[31] By lowering the pillar diameter to 1.4 μm , in combination with quasi-static strain rates between 10^{-4} and 10^{-3} s^{-1} , anomalous plastic strains of up to 60% can be produced.^[22] However, again almost all the pillars typically fail during loading or at the onset of unloading, and increasing the strain rate to 10^{-1} s^{-1} or above lowers the achievable strain-to-failure back to 20%–40%.^[22] Densification of a-SiO_2 can facilitate a large portion of the measured strain in the compressed micropillars, while changing the diameter-to-height ratio can alter the cracking behavior in the pillars by limiting the maximum tensile hoop stress obtained along the circumference of the pillars.^[32] Although microcompression of a-SiO_2 indicates potential damage tolerance,

F. Di Fonzo
X-nano s.r.l
Via Rubattino 8, Milano 20134, Italy

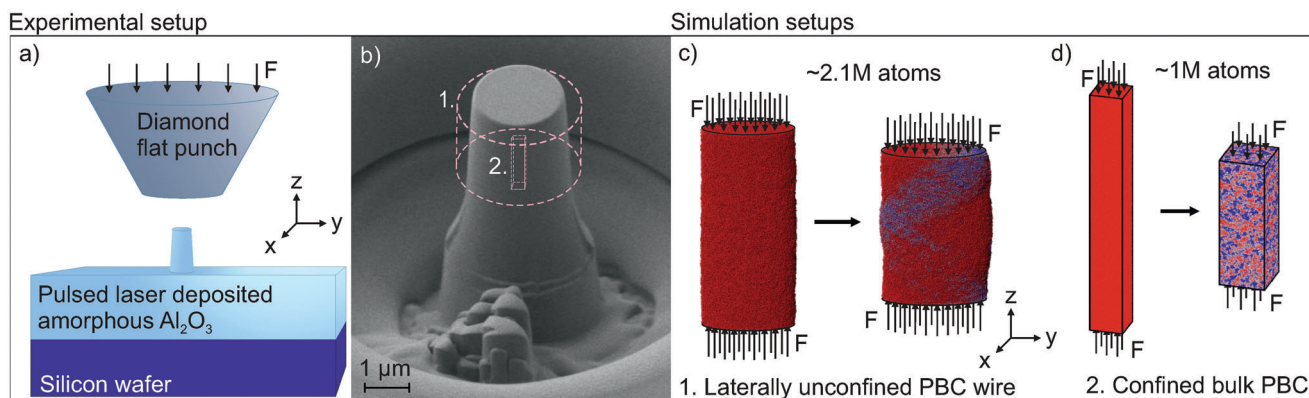


Figure 2. Experimental and simulated micropillar compression of a- Al_2O_3 at room temperature (≈ 300 K). a) Schematic picture of the micropillar compression experiment utilizing in situ measurement of force and displacement. b) An as-milled a- Al_2O_3 micropillar imaged using scanning electron microscopy. c) A ≈ 2.1 M atom molecular dynamics simulation “wire” model of a- Al_2O_3 to simulate the laterally unconfined conditions (periodic boundary condition (PBC) applied in the z-direction) prevailing in the micropillar body under uniaxial compression, with an initial cell diameter of ≈ 24 nm and length of 50 nm. d) A ≈ 1.0 M atom molecular dynamics simulation for a “bulk” model of a- Al_2O_3 to simulate the confined bulk plastic deformation mechanisms active inside the micropillar during uniaxial compression (PBC applied in x-, y-, and z-directions), with initial cell dimensions of $\approx 11 \times 11 \times 90$ nm.

pure tensile stress in a- SiO_2 always produces an elastic brittle fracture without plasticity,^[12,33] excluding certain anomalies observed in the extreme nanoscale.^[34] In addition to a- SiO_2 , metal-organic framework glasses have been shown to exhibit significant densification-driven plasticity under microcompression,^[35] however, similar to bulk glassy SiO_2 , a melt-quenched bulk MOF glass is shown to remain brittle.^[36]

Here we provide evidence that the plasticity phenomenon observed earlier in a- Al_2O_3 thin films extends to the microscale and high strain rates. We do so by using combined micropillar compression experiments and molecular dynamics (MD) simulations supported by finite element method (FEM) modeling. The total volume of a- Al_2O_3 samples undergoing significant plasticity without fracture is increased from the earlier discovery by five orders of magnitude from 10^7 nm³ to 10^{12} nm³.^[12] Simultaneously, the highest experimental strain rate possible to be used without fracture is shown to be extended by four orders of magnitude up to 10^3 s⁻¹ when compared to previous results limited to 10^{-1} s⁻¹.^[12] We show that a- Al_2O_3 exhibits exceptional plasticity in the realm of ceramic and oxide glass micropillar compression, exhibiting plastic strain of up to 50%, and, in contrast to a- SiO_2 , it deforms without any fracture during loading or unloading. We show that the observed plasticity in a- Al_2O_3 is not due to any size or strain rate effects known in the literature to possibly influence such results. So far, all improvements in oxide glass damage tolerance have been related to producing stronger glasses, for example, by inducing residual stresses or producing more elastically flexible glasses by limiting the glass film thickness.^[37] Here, we introduce a new functionality to ceramic and glassy oxide materials: a ductile response to mechanical loading.

2. Results

We performed in situ micropillar compression experiments and large-scale atomistic simulations to study the microscale plasticity of a- Al_2O_3 at room temperature (≈ 300 K) (Figure 2). The micropillar compression setup induces unconfined and complex

loading on the sample including compressive, shear, tensile, and hydrostatic loading components, at any given strain and often simultaneously. Residual stresses created during the PLD synthesis are relieved on the micropillar samples due to the milling process and are therefore not considered to impact the results. The PLD process was optimized to enable the growth of a- Al_2O_3 films up to 50 μm thick with a minimal defect size and defect density. For detailed characterization of microstructures and chemical composition see supplementary Section S1, Supporting Information.

Plasticity without fracture was observed in all performed experiments and simulations. Figure 3a summarizes a set of representative experimental stress-strain results of up to $\approx 20\%$ compressive strain at strain rates varying between 10^{-3} and 10^3 s⁻¹ (for the full data set including data from all 21 micropillars, see supplementary Section S2, Supporting Information). The end of the experiment is indicated by the relaxation of stress back to ambient pressure. In Figure 3b, we show the MD simulated compressive stress-strain response of a- Al_2O_3 with “bulk” and “wire” setups with up to $\approx 40\%$ strain, including multiple relaxations back to ambient pressure in the bulk setup (1 atm at 20%, 30%, and 40% strain).

In all the experimental and simulated loading scenarios, at the onset of loading, the material first responded with reversible elastic strain. As the stress increased, an irreversible plastic yielding gradually initiated along with a transition from elastoplastic to plastic yielding. When the externally applied stress overcame the strength of the material, the stress reached a maximum, which we define as yield stress. After yield stress, a relaxation of the stress occurs, and the stress slightly decreased until leveling to a constant value, which we define as flow stress. The gradual increase of engineering flow stress as a function of strain appearing in Figure 3a-b does not originate from the hardening of the material, nor from a changing strain rate, but experimentally originates from the initial pillar taper, i.e., the pillar has a larger diameter in the lower part. The simulated true stress, which considers the momentary change in sample diameter, confirms the lack

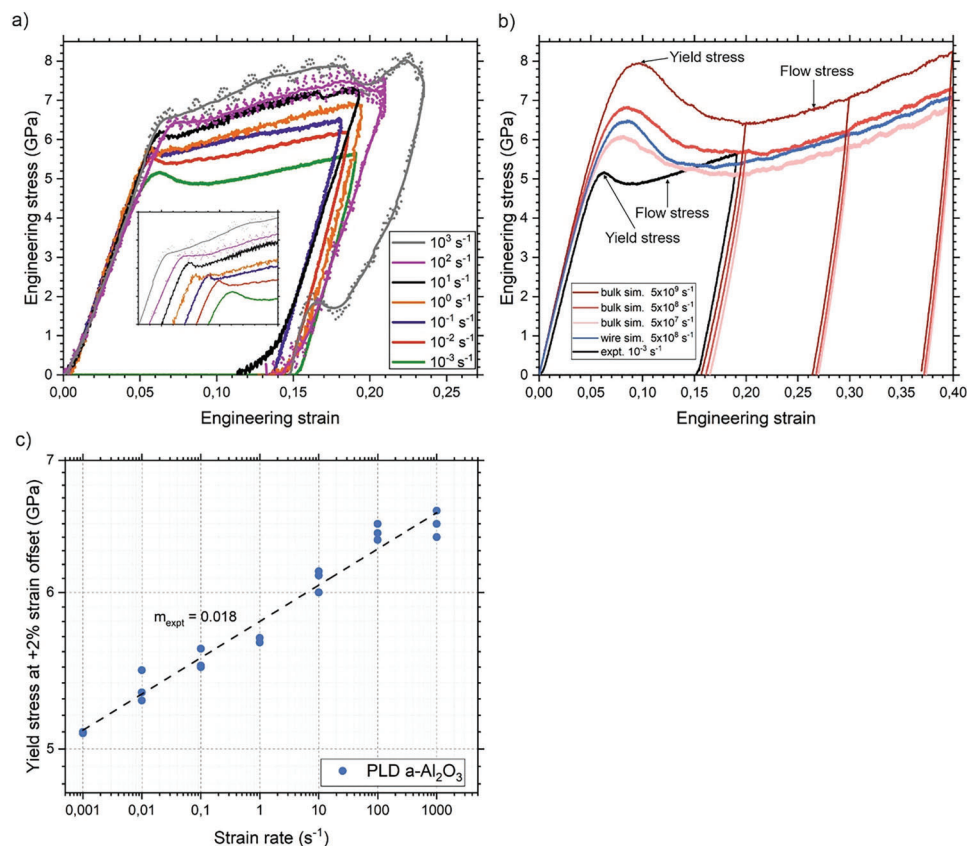


Figure 3. Dynamic mechanical response of a-Al₂O₃ using micropillar compression and molecular dynamics simulations at room temperature (≈ 300 K). a) Engineering stress as a function of engineering strain in micropillar compression at different strain rates, with an inset zooming in on the yield stress region with a 2% strain offset for clarity ($\dot{\epsilon} = 10^{-3}$ – 10^3 s⁻¹, $n = 1$, where $\dot{\epsilon}$ is strain rate, and n is the number of samples averaged for each data point/plot); for samples strained at 10^2 s⁻¹ and 10^3 s⁻¹, adjacent average plot smoothing is shown using 20 points of the window with Origin software. b) Engineering stress as a function of engineering strain in confined bulk PBC simulations of a-Al₂O₃ with varying strain rates ($\dot{\epsilon} = 5.00 \times 10^7$ s⁻¹, 5.00×10^8 s⁻¹, 5.00×10^9 s⁻¹, $n = 1$), in a laterally confined PBC wire simulation ($\dot{\epsilon} = 5.00 \times 10^8$ s⁻¹, $n = 1$), and in comparison to experimental mechanical behavior ($\dot{\epsilon} = 10^{-3}$ s⁻¹, $n = 1$). c) Log-log presentation of the micropillar yield stress data at 2% strain offset as a function of strain rate to determine the strain rate sensitivity m_{expt} for a-Al₂O₃ ($\dot{\epsilon} = 10^{-3}$ – 10^3 s⁻¹, $n = 1$).

of strain-hardening mechanisms as true flow stress remains approximately constant (see Section S3, Supporting Information). Amorphous Al₂O₃ is a strain rate-sensitive, or viscous, material, meaning that increasing the strain rate increased both the yield stress and flow stress, and vice versa, in both the experiments and simulations. The strain rate sensitivity factor m was measured to be 0.018 (Figure 3c), and the linear fit in the log-log plot of m indicates that the overall plasticity mechanism did not change even when scanning the strain rate between 7 orders of magnitude. As the experiments and MD simulations, both show a remarkably similar mechanical response for a-Al₂O₃ (Figure 3b), despite the large difference in strain rates, we used the simulations to investigate the plausible atomistic mechanisms enabling the microscale plasticity.

The experimental and MD simulated stress-strain behavior (Figure 3), ex situ images of the compressed micropillars (Figure 4) supported by FEM modeling (Figure 5), and the analysis of MD-straining simulations (Figure 6) reveals a mechanism of microscale plasticity for a-Al₂O₃ at room temperature comprising two phenomena: 1) homogenous viscous creep through fast nucleation of localized plastic strain events (LPSE, see definition

in Frankberg et al.^[12]) and 2) localization of the LPSE nucleation to narrow, $\approx 45^\circ$ angle bands, commonly known as shear bands (SBs), and the slip-like propagation of shear deformation along these bands. For a-Al₂O₃ in compression, the permanent density increase associated with the LPSE-mediated viscous creep mechanism gives a negligible contribution to the measured plastic strain and is not considered here as a significant mechanism to contribute to the plastic strain (see Section S4, Supporting Information). First, regarding the evidence for the proposed plasticity mechanism, we discuss the atomistic simulations.

2.1. Molecular Dynamics Simulations

The MD simulations were analyzed using the D_{min}^2 , a descriptor for local atomic plastic strain described by Falk and Langer.^[38] Plastic strain in a-Al₂O₃ is known to be mediated by atoms exhibiting above-average D_{min}^2 values.^[12] Here, the LPSE is defined as an atom cluster comprising of at least 200 atoms that all exhibit D_{min}^2 of at least twice the average value determined over

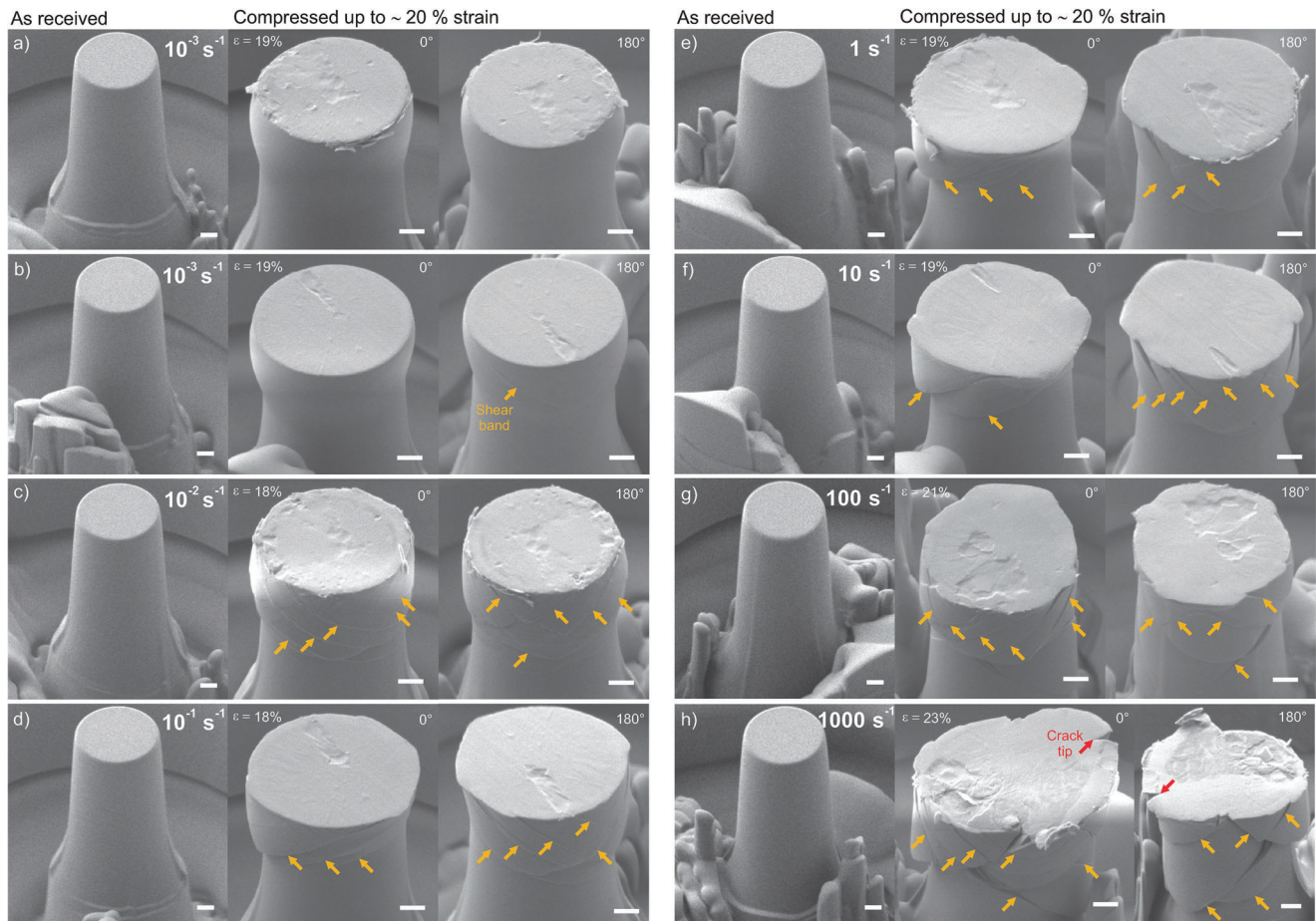


Figure 4. Micromechanical response of α - Al_2O_3 at room temperature. a) Micropillar R1C4 strained by 19% at 10^{-3} s^{-1} strain rate, b) R2C3 strained by 19% at 10^{-3} s^{-1} , c) R1C3 strained by 18% at 10^{-2} s^{-1} , d) R2C1 strained by 18% at 10^{-1} s^{-1} , e) R1C6 strained by 19% at 1 s^{-1} , f) R2C5 strained by 19% at 10 s^{-1} , g) R4C4 strained by 21% at 100 s^{-1} , h) R3C1 strained by 23% at 1000 s^{-1} . The first sub-image shows the as-prepared micropillar, the second sub-image shows the deformed pillar rotated 180° . The orange and red arrows show the locations of shear bands and crack tips, respectively. The scale bar is 400 nm.

the whole system (see Figure 6a,c and Section S6, Supporting Information). The bond-switching mechanism that mediates the LPSE nucleation was earlier introduced in detail by Frankberg et al.^[12]

First, we simulated the compression of a fully confined bulk α - Al_2O_3 by enforcing periodic boundary conditions on all axes (Figure 2d). This simulation setup allows us to observe plasticity phenomena occurring inside the experimental micropillar, a confined volume under uniaxial compression. These simulations reveal that the plasticity initiates and endures by nucleation of LPSEs that dynamically shift location with each measured strain step (Figure 6a, Movie S1, Supporting Information). The nucleation rate of the LPSEs is shown to reflect the measured stress-strain behavior of α - Al_2O_3 , as is quantitatively depicted in Figure 6e. The figure indicates that the nucleation of LPSEs initiates during the elastoplastic phase before full yielding and the nucleation reaches the maximum level after the yield stress. As the LPSE nucleation starts increasing, the slope of the stress-strain curve starts simultaneously decreasing, and, therefore, reveals the connection between stress and LPSE activity. After relaxing the excess elastic energy, the LPSE nucleation rate gradually de-

creases until a steady state level, which occurs in parallel with the leveling of the true stress. The LPSEs continue to nucleate at up to 50% strain without any obvious pattern, which leads to a largely homogenous distribution of the cumulative local plastic strain (Figure 6b, supplementary movie S2, Supporting Information). In addition, there is a noticeable degree of localization to the band-like collection of atoms that measure above-average cumulative D^2_{min} . These band-like patterns, however, do not exclusively form in the characteristic 45° angle with respect to the axis of compression, which is typically associated with the formation of SBs.

Second, to understand the role that free surfaces have in the microscale plasticity, we simulated the compression of laterally unconfined α - Al_2O_3 wire with α - Al_2O_3 /vacuum interfaces imposed on the x - and y -axes. This corresponds to a miniature experimental micropillar under uniaxial compression, with a diameter ratio of $\approx 1:194$ between the experiments and simulations shown in Figure 2. During the elastoplastic response occurring before yielding $\epsilon \approx 0.01$ – 0.08 , the LPSEs nucleate sporadically with each strain step up to the yield stress (Figure 6c, Movie S3, Supporting Information) in a similar manner as in the bulk simulations.

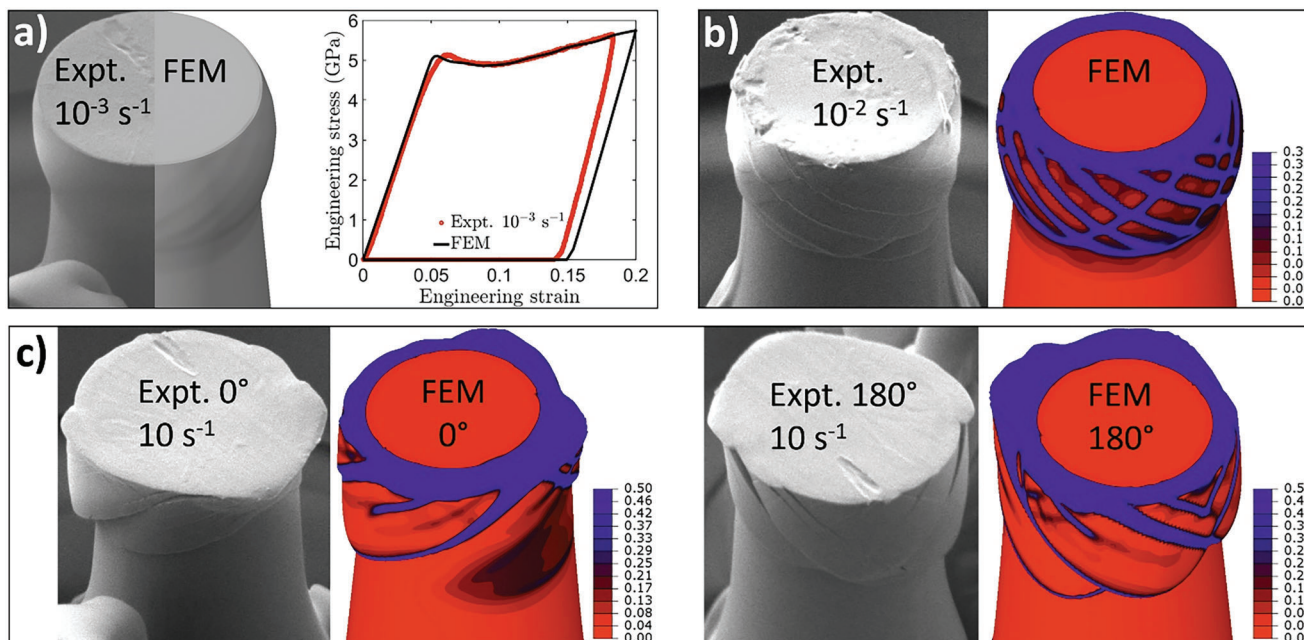


Figure 5. Finite element modeling of α - Al_2O_3 at room temperature. a) The pillar's deformed shape, which is produced by a homogeneous viscous creep mechanism at a 10^{-3} s^{-1} strain rate (left), is reproduced by the FE model (right) using a set of damage-related parameters associated with the experimental strain rate, and the comparison of experimentally measured ($\dot{\epsilon} = 10^{-3} \text{ s}^{-1}$) and FEM-simulated engineering stress as a function of engineering strain. b) Pillar deformed shape governed by a mixture of homogeneous viscous creep and shear band localization at a 10^{-2} s^{-1} strain rate (left) is reproduced by the FE model (right) using a set of damage-related parameters associated with the experimental strain rate. c) The shift towards shear band propagation dominated plasticity at a 10 s^{-1} strain rate is qualitatively captured by the FE model using a set of damage-related parameters associated with the experimental strain rate; images from the same sample with left-side images rotated 0° and right-side images rotated 180° . The legends show the spectrum of scalar stiffness degradation (SDEG) or damage. More details on the developed finite element model can be found in Section S5, Supporting Information.

However, a transition occurs at a yield stress $\epsilon \approx 0.09$, where the LPSE nucleation and the overall plasticity localize on shear bands emerging at a characteristic $\approx 45^\circ$ angle (D_{\min}^2 , $\epsilon = 0.20$, $\Delta\epsilon = 0.01$, Figure 6c, Movie S3, Supporting Information). A larger collection of LPSEs appear to nucleate at the intersections of the two colliding SBs. The shifting LPSEs form networks of continuous plastic strain, resulting in a mechanism for the slip-like propagation of SBs observed in the experimental samples in Figure 4; however, the simulations do not show displacement steps forming at places where SBs intersect with the simulation sample surface, as the SB is not able to break the surface tension. This is possibly due to the small model structure restricting the formation and propagation of SBs or the periodicity along the z -axis, which inhibits the relative displacement of the model's top and bottom surfaces along the xy -plane (geometrically required for the steps to appear). It is also possible that the collision between the two SBs inhibits a step from initiating. SBs initiate and intersect with sample surfaces at $\approx 45^\circ$ with respect to the compression axis because the shear stress maximum occurs at this angle.^[39] The cumulative plastic strain shows that as soon as the SBs begin to form, most of the plasticity is concentrated in them, and atoms residing in the volume left between the SBs and pillar surfaces remain relatively stationary, with a minor plastic strain (D_{\min}^2 , $\epsilon = 0.20$, $\Delta\epsilon = 0.20$, Figure 6d, Movie S4, Supporting Information).

At higher strains nearing 50%, the LPSE nucleation returns to cover more homogeneously the PBC wire sample volume (D_{\min}^2 , $\epsilon = 0.47$, $\Delta\epsilon = 0.01$, Figure 6c, Movie S3, Supporting Informa-

tion). This most likely occurs due to the large change in the diameter/height ratio, altering the stress state occurring in the material. At this stage, however, most of the cumulative local plastic strain (D_{\min}^2) has already localized at the intersections between the dominant SBs (D_{\min}^2 , $\epsilon = 0.47$, $\Delta\epsilon = 0.47$, Figure 6d, Movie S4, Supporting Information). The D_{\min}^2 parameter analysis for local plastic strain irrevocably shows that the LPSE nucleation mechanism remains active during the whole straining, and therefore also the SB slip occurs via LPSE nucleation. This is supported by the fact that no significant changes occur in the stress-strain behavior of the materials between different atomistic models, and that there are no changes in the strain-rate sensitivity, indicating a possible change in the mechanism (Figure 3). However, due to the required transition from homogenous viscous creep to localized SB propagation, plastic strain induced by LPSE nucleation localizes to a specific volume that exceeds the yield stress, *i.e.*, the active plastic volume, which appears as a narrow band in the case of SBs.

2.2. Micropillar Compression

The ex situ images of the compressed pillars depict how the plastic strain can be distributed homogeneously across the whole active plastic volume (Figure 4a) or localized to shear bands (Figure 4h). However, we show how these two phenomena are highly intertwined parts of the same plasticity

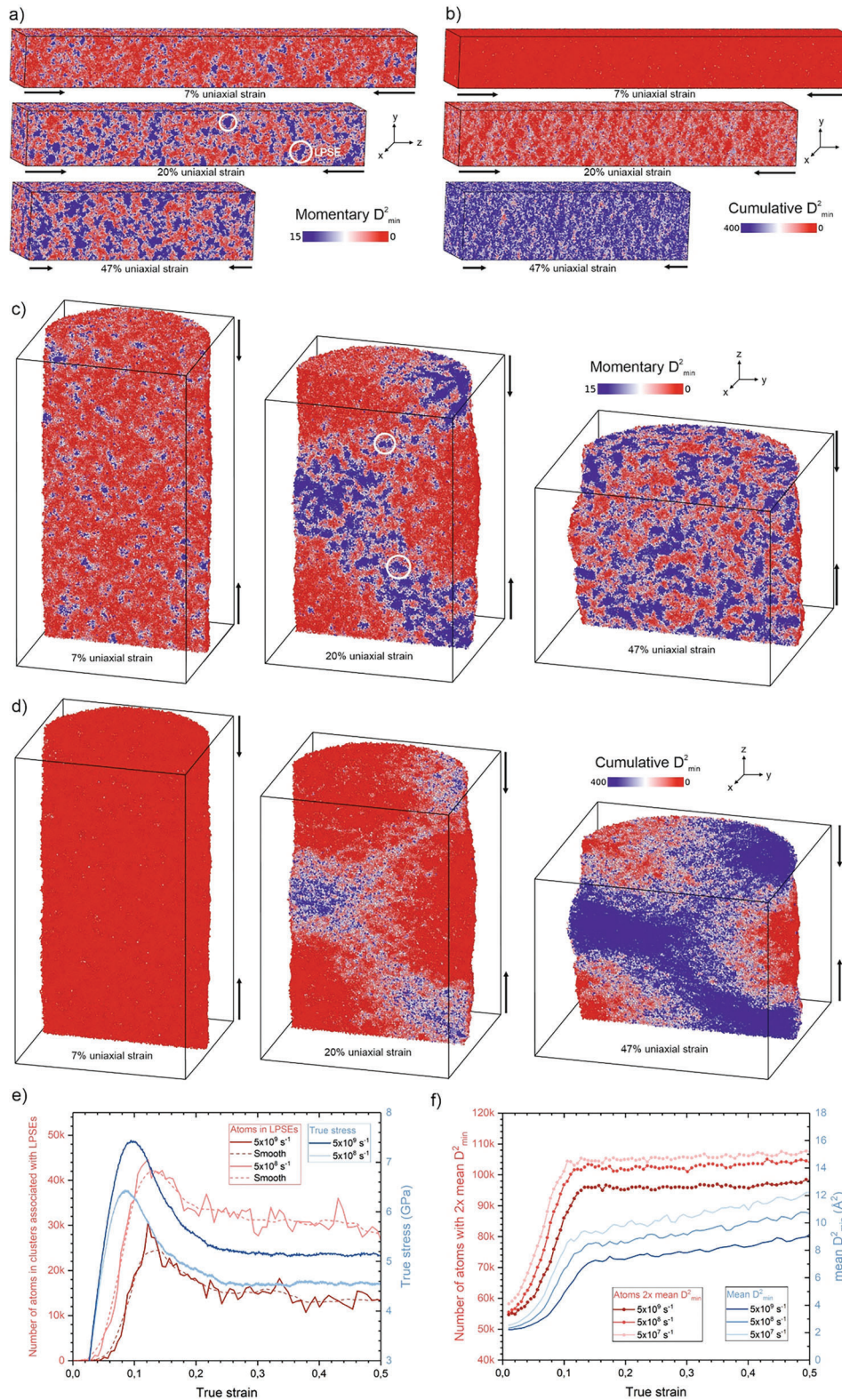


Figure 6. Plasticity mechanism in α - Al_2O_3 at room temperature (300 K) using molecular dynamics simulations. a, b) Confined bulk PBC simulations under uniaxial compression measured at $\epsilon = 0.07$, $\epsilon = 0.20$, and $\epsilon = 0.47$, a) with the momentary distribution of local plastic strain (D_{\min}^2 , $\Delta\epsilon = 0.01$, $\dot{\epsilon} = 5 \times 10^8 \text{ s}^{-1}$) and b) with the cumulative distribution of local plastic strain (D_{\min}^2 ; $\Delta\epsilon = 0.07$, $\Delta\epsilon = 0.20$, $\Delta\epsilon = 0.47$, $\dot{\epsilon} = 5 \times 10^8 \text{ s}^{-1}$), where ϵ is strain and $\Delta\epsilon$ indicates the reference frame for the D_{\min}^2 calculations. c, d) Vertical cross-sections of laterally unconfined PBC wire simulations under uniaxial compression measured at $\epsilon = 0.07$, $\epsilon = 0.20$, and $\epsilon = 0.47$, c) with the momentary distribution of local plastic strain (D_{\min}^2 , $\Delta\epsilon = 0.01$, $\dot{\epsilon} = 5$

mechanism mediated by nucleation and the accumulation of LPSEs, contributing to the damage resistance of $\alpha\text{-Al}_2\text{O}_3$ in varying proportions.

In the micropillar compression experiments performed at slower strain rates of 10^{-3} s^{-1} – 10^{-2} s^{-1} , the homogenous nucleation of LPSEs, *i.e.*, viscous creep, dominated as the source of measured plastic strain. At the slowest experimental strain rate 10^{-3} s^{-1} , none or only a singular SB slip can be seen to have propagated with a minor displacement, as seen in the ex situ images of the pillars strained to $\approx 20\%$ (Figure 4a–b). The mechanical response at low strain rates correlates well with the bulk simulations (Figure 2d, Figure 6a–b), in which the plasticity occurs mainly by the homogenous nucleation of LPSEs. In addition to the lack of significant contribution of SBs, the LPSE nucleation-driven plasticity induces a distinct “barreling” of the pillar shape, where the ex-situ pillar body diameter exceeds the top face diameter (Figure 4a–c). The barreled ex-situ micropillar shape can be fully replicated by an FEM model combining the Von Mises (metal) plasticity with shear damage constitutive behavior when choosing damage parameters that allow the plastic deformation to be more homogeneously distributed across the pillar’s active plastic volume,^[40,41] with only a minor contribution from strain localization to SBs (Figure 5a, Figure S5.2e, Figure S5.3a–c, Section S5, supplementary Movie S5, Supporting Information).

When increasing the experimental strain rates, fewer LPSEs nucleate homogeneously in the whole volume. Instead, an increasing amount of LPSEs localize on SBs and the slip-like propagation of SBs begins to contribute more to the overall plastic strain. When changing the experimental strain rate through 10^{-3} s^{-1} to 10^{-2} s^{-1} and to 10^{-1} s^{-1} , a transition gradually occurs where the localized slip-like propagation of SBs increases and gradually takes over as the main mechanism inducing plastic strain when further shifting to higher strain rates. Multiple SB slips can be seen to have propagated at the strain rate of 10^{-2} s^{-1} in the ex situ image of the strained pillar (Figure 4c). However, the dislocation length of each SB is still relatively small and a distinct barreling of the pillar remains evident, indicating that the plasticity still mostly occurs homogeneously in the deformed volume and is dominated by the sporadic nucleation of LPSEs. The FEM model cross-section confirms that minor SB localization can occur at the pillar surfaces, while the majority of the plastic strain still occurs homogeneously in the active plastic volume inside the pillar, and hence the pillar obtains a barrel-like shape when deformed (Figure 5b, Figure S5.3, Supporting Information).

The transition from the homogenous LPSE-driven plasticity to the SB slip propagation-driven plasticity occurs at strain rates between 10^{-1} s^{-1} to 1 s^{-1} , and accordingly, the strain-induced barreling of the pillar transforms into strain-induced “mushrooming” of the pillar, *i.e.*, the diameter of the pillar top face overcomes

the pillar body diameter as observed in the ex situ images of the strained pillars (Figure 4d–e). The SB slips begin to show a larger overall displacement in the ex situ pillar images, which is displayed as a measurable displacement step between the propagated SB and the body of the pillar (Figure 4f–g, SBs and steps indicated with arrows). The atomistic simulations using the unconfined wire geometry (Figure 2c) confirm that at high strain rates, the plasticity concentrates on a few dominant SBs tilted at a $\approx 45^\circ$ angle with respect to the strained axis (Figure 6c–d). We then change the FEM damage model parameters to account for the change in the dominant plasticity phenomenon. The modified FEM model can reproduce the transition from homogenous viscous creep plasticity to a more localized SB slip propagation-driven plasticity and the following mushroom shape of the pillar as a consequence of this transition (Figure 5c, Figure S5.3e–f, Section S5, Movies S6–S7, Supporting Information). As the strain rate is further increased to 10^1 – 10^3 s^{-1} , a gradual shift to increasingly SB slip propagation-dominated plasticity can be observed (Figure 4f–h), however, without any sudden load drops associated with fracture (Figure 3a, Figure S2, Supporting Information). In addition to SBs, cracks begin to appear at the highest strain rates (Figure 3h). However, the focused ion beam sectioning done on a sample deformed at 10^2 s^{-1} shows that the cracking is mostly restricted to the outer surfaces of the pillar, penetrating inwards up to a few hundred nanometers, while the inner parts of the pillars continue to deform homogeneously without defects (see Section S1, Supporting Information).

2.3. Origin of the Plasticity

The MD simulation results suggest that the nucleation of LPSEs is a rate-limited mechanism, as creep generally is. This requires that if the prevailing temperature remains constant, the nucleation occurs at an approximately constant rate independent of the strain rate, therefore limiting the amount of available atom translocations. Increasing the strain rate gradually forces the momentarily available LPSEs to concentrate increasingly on the few dominant shear bands to allow the geometrically required plastic strain without fracture. To confirm the constant rate hypothesis, we performed simulations at different strain rates, while mapping the occurrence of atoms exhibiting a high D^2_{min} (Figure 6f). The results confirm that at a constant temperature, the total amount of these highly mobile atoms changed only by 2%–4% when the strain rate increased or decreased by an order of magnitude. The rate-limited nucleation of LPSEs serves as a further indication of the diffusion-based origin of the viscous creep mechanism discussed earlier by Frankberg et al.,^[12] and it ultimately causes the $\alpha\text{-Al}_2\text{O}_3$ to exhibit a strain rate-sensitive mechanical response to loading. Despite of the relatively constant nucleation rate, the atomistic simulations confirm that the bond switch-driven nucleation of LPSEs remains highly active in $\alpha\text{-Al}_2\text{O}_3$ at all

$\times 10^8\text{ s}^{-1}$) and d) with the cumulative distribution of local plastic strain (D^2_{min} ; $\Delta\epsilon = 0.07$, $\Delta\epsilon = 0.20$, $\Delta\epsilon = 0.47$; $\dot{\epsilon} = 5 \times 10^8\text{ s}^{-1}$). e) Nucleation rate of LPSEs (left y-axis) and true stress (right y-axis) as a function of true strain in confined bulk PBC simulations ($\dot{\epsilon} = 5 \times 10^8\text{ s}^{-1}$ – $5 \times 10^9\text{ s}^{-1}$, $n = 1$). f) Total amount of atoms in the confined bulk PBC simulations exhibiting a degree of local plasticity two times the mean D^2_{min} (left y-axis) and the mean D^2_{min} (right y-axis) as a function of strain at varying strain rates ($\dot{\epsilon} = 5 \times 10^7\text{ s}^{-1}$, $5 \times 10^8\text{ s}^{-1}$, $5 \times 10^9\text{ s}^{-1}$, $n = 1$). Using a sliding color scale, atoms with below-average D^2_{min} are shown in shades of red, average D^2_{min} are white, and above-average D^2_{min} are shades of blue. All atoms above the color scale are also in blue. Examples of LPSE clusters are indicated by white circles in (a) and (c). Loading axes are indicated by arrows.

strain rates. The nucleation occurs at a fast enough rate to play an important role in preventing the catastrophic propagation of the dominant SB slip, which is a known fracture mechanism in brittle metallic glasses.^[39,42] Based on the rate-limited nucleation of LPSEs, we will next explain the origin and shape of the a-Al₂O₃ stress-strain curve.

As further evidence of the viscous origin of the stress-strain behavior in a-Al₂O₃, the experimental and simulated data indicate that the magnitude of the stress is dependent on the strain rate resulting in a non-Newtonian response: Both yield stress and flow stress increase when the strain rate is increased (Figure 3a-b). Simultaneously the ratio between the stress and strain rate decreases, resulting in decreased viscosity, and the reverse is true when the strain rate is decreased, following closely the behavior reported for a-Al₂O₃ earlier.^[12] The strain rate-dependent behavior of a-Al₂O₃ micropillars under compression was further studied using a dedicated strain rate jump test (see Section S7, Supporting Information), which confirmed the viscous, strain rate-sensitive response to the applied load. The experimental strain rate sensitivity (*m*) of flow stress (σ) was determined to be 0.018 (Figure 3c). The micropillar strain rate jump test yielded an instantaneous strain rate sensitivity $m = 0.025 \pm 0.003$, confirming the constant strain rate measurements shown earlier, and an apparent activation volume of $0.05 \pm 0.007 \text{ nm}^3$ from the data shown in supplementary Figure S7.1 via Equations S7.1 and S7.2, Supporting Information. To compare, the apparent activation volume of a-Al₂O₃ is an order of magnitude smaller compared to the typical activation volume observed in metallic glasses.^[43] This suggests a deformation mechanism that operates over a smaller volume than in some metallic glasses, which are described to deform by local rearrangement of atoms within shear transformation zones. The smaller activation volume is also in line with the atomistic bond-switching mechanism suggested for a-Al₂O₃ earlier by Frankberg et al.^[12]

Regarding the shape of the stress-strain curve, the yielding occurs at a higher stress level, while the steady-state flow after yielding occurs typically at a lower stress level (Figure 3a-b). This “hump” in the stress data originates from the atomic arrangement occurring in the quenched glassy structure and occurs in both the PLD material transiting from gas to solid state and in simulated cast-quenched material transiting from liquid to solid state. The quench rate in the PLD technique is estimated to reach up to 10^{13} K s^{-1} ,^[44] and our simulated quench rate for both confined bulk and laterally unconfined wire setups was $3.6 \times 10^{12} \text{ K s}^{-1}$. These high cooling rates form a structure that is over-relaxed and exhibits a potential well, which requires extra energy to allow for the flow of atoms to start, analogous to the static friction phenomenon at the molecular level.^[33,45] To confirm this hypothesis, we performed an additional simulation where the quench rate approaches infinity and therefore avoids the formation of the potential well (see Section S8, Supporting Information). This resulted in a sharp transition from elastic to plastic yielding, without the stress hump, and confirmed the hypothesis regarding the origin of the hump. The extra elastic energy needed to overcome the potential well is released at yielding and briefly enhances the nucleation of LPSEs (Figure 6e) until reaching a lower potential energy arrangement of atoms and a steady state flow with a level true stress and a level overall LPSE nucleation rate (Figure 6e). The stress hump appears to be specif-

ically related to the non-localized LPSE nucleation, since if we experimentally increase the strain rate, the size of the hump decreases as the localized SB slip propagation becomes more predominant in inducing the plastic strain (Figure 3a). In all performed simulations, the propagation of SBs appeared restricted and therefore the hump is clearly visible in both simulation setups and at all strain rates. Additionally, the micropillar strain rate jump test allowed the observation of the stress hump multiple times during a single compression experiment, and it occurred only after increasing the strain rate, but not when decreasing the strain rate (Figure S7.1, Supporting Information). This implies that mechanical activation is equally capable of inducing viscous relaxation of the a-Al₂O₃ amorphous atom network, and when shifting from a lower to higher strain rate, a phenomenon similar to a thermal quench occurs, creating a potential well that needs to be overcome due to atoms residing in overrelaxed positions. Therefore, we can also hypothesize that the potential energy for atom bond switching, i.e., the activation energy for plasticity, is strain-rate-dependent and increases with the strain rate.

In an attempt to fracture the a-Al₂O₃ micropillars, we performed experiments where the maximum strain was increased up to 39%–51% (Figure 7a-c). We did not detect fracture or loss of cohesion in any of the samples either during loading or unloading, despite the large displacement of SB slips during the highest strain rate tests, and the apparent crack formation at the intersection between SBs and the pillar top surface shown in Figure 7b-c, and Figure S1.2, Supporting Information, (for stress-strain data, see supplementary Section S2, Supporting Information). The results align with the test performed to lower maximum strain: the viscous creep remains the controlling mechanism for plasticity at a lower strain rate (Figure 7a, 10^{-2} s^{-1}), while the SB propagation becomes the main driving mechanism for plasticity at the highest strain rates (Figure 7b-c, 1000 s^{-1}). The highly strained samples confirm the active role of LPSE nucleation in containing damage and suppressing fracture, and despite the large slip-like deformation along the dominant SBs, the samples maintain their cohesion and load-bearing capacity. The deformed samples appear smeared, i.e., deformed in a similar manner to highly plastic materials, such as molding clay or polycrystalline gold. Shear band propagation alone cannot produce such smeared surfaces, and therefore the overall plastic strain on the microscale is accommodated via an interplay between the nonlocalized LPSE nucleation and SB propagation via localized LPSE nucleation up to a 1000 s^{-1} strain rate and beyond, as the simulations suggest. Further, in an attempt to produce a fracture in the PLD a-Al₂O₃ micropillar, we produced and tested larger pillars with up to 11 μm in diameter, with a strain rate of 10^{-2} s^{-1} , to study whether the observed plasticity is a size-effect, i.e., related to the size of the micropillars, and whether it would be possible for the plasticity to be scaled further towards bulk. The results show that also these pillars deform up to 20%–38% strain without failure (Figure 7d, for additional data see Section S9, Supporting Information). As introduced earlier, this behavior is exceptional compared to the available literature on both crystalline and amorphous ceramics, including semiconductors, and it aligns with the theoretical prediction by Frankberg et al. that the viscous plasticity mediated by fast LPSE nucleation can be scaled to flaw-free, bulk oxide glasses. The results also suggest that it is plausible to synthesize such adequately flaw-free samples on a larger scale to test the hypothesis.

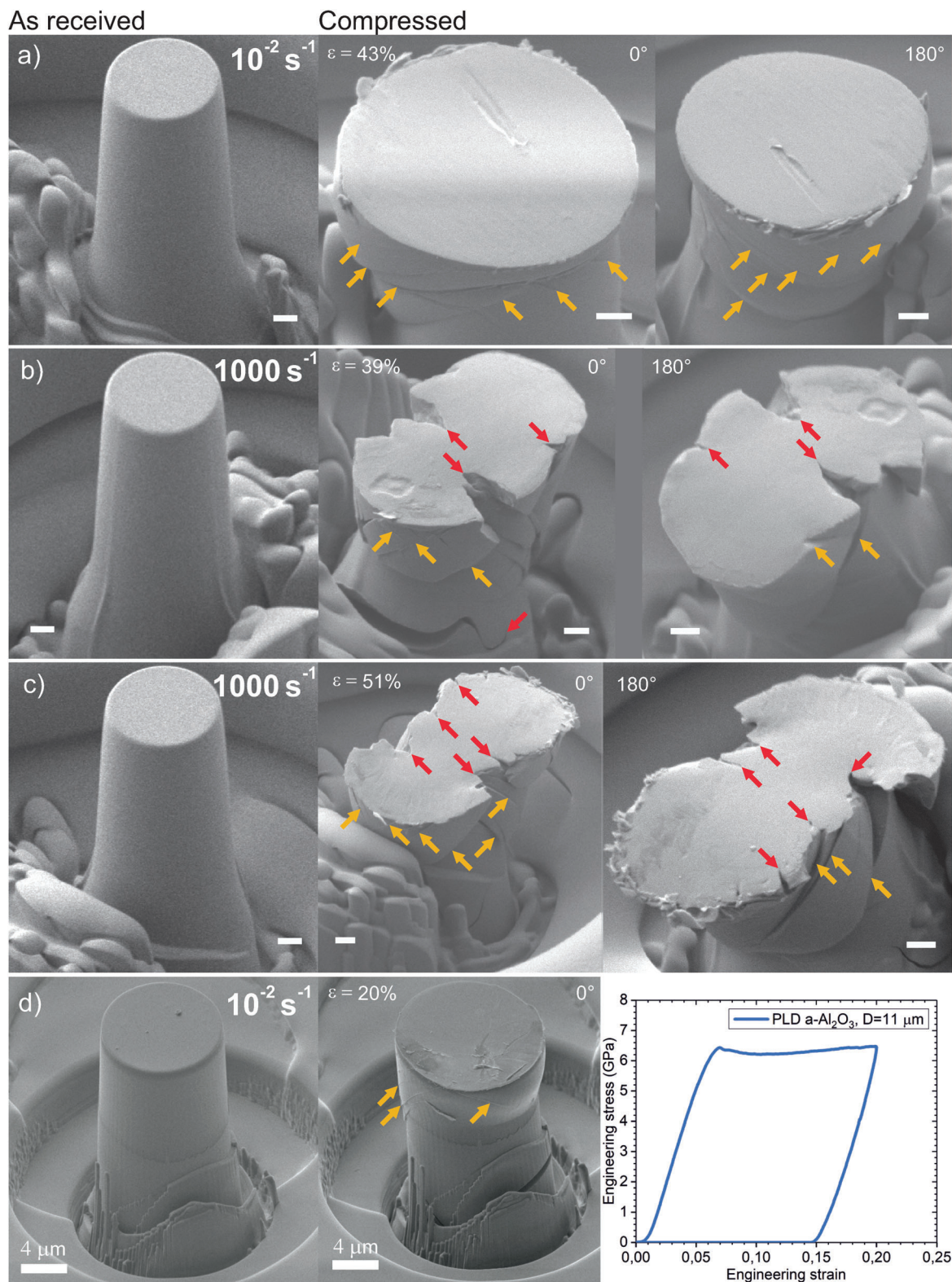


Figure 7. Plastic deformation without fracture in α - Al_2O_3 micropillars with a high strain and larger pillar diameter. a) R3C3 strained to $\approx 43\%$ at 10^{-2} s^{-1} , b) R4C3 strained to 39% at 1000 s^{-1} , c) R4C1 strained to 51% at 1000 s^{-1} , d) a larger micropillar, with diameter $D \approx 11 \mu\text{m}$, strained to 20% at 10^{-2} s^{-1} and stress-strain data showing the mechanical response of the pillar during loading and unloading. The first sub-image shows the as-prepared micropillar and the consecutive sub-images show the deformed pillar at a given direction of view (0° or 180°) or the stress-strain behavior. The arrows indicate the location of shear bands (orange) and crack tips (red). The scale bars are 400 nm and $4 \mu\text{m}$.

3. Discussion

We have shown that a-Al₂O₃ plasticity extends to the microscale, but a profound question still remains: why does a-SiO₂, the prototypic glass former, remain brittle? Although a-SiO₂ shows a considerable amount of ductility on the nano and microscale, the literature indicates that it can be considered mainly as anomalous behavior, e.g., plasticity has been observed in the presence of an electron beam,^[34,46] the simulated atom structure is artificially densified before straining to allow plasticity,^[47] or the plasticity in micropillar compression is caused by the small sample volume and the compressive stress delays crack propagation, and at the latest the fracture typically occurs once the load is released.^[22,31] No experimental data on a-SiO₂ micropillars larger than $D > 3.1 \mu\text{m}$ tested under ambient conditions have been published to our knowledge. Excluding these anomalous cases, there are no indications that the plasticity of pure a-SiO₂ could even theoretically extend to the bulk scale. Atomistic simulations show that unconfined tensile and shear stresses tend to nucleate cracks even in the pristine quenched a-SiO₂ structure, eventually leading to fracture.^[33,48] Nevertheless, studying plasticity and fracture in a-SiO₂ remains important. To learn how to produce ductile oxide glasses, we have to understand why the most common glass former remains brittle at a low temperature.

Shear band nucleation and their slip-like propagation is a known and important plasticity mechanism in amorphous metals (bulk metallic glasses) and amorphous oxides alike.^[22,39,41,42] In a-Al₂O₃ the importance of SBs is also clear based on the current results: At higher strain rates, an increasing portion of the measured plastic strain is caused by SB slip, and at the extreme strain rate of 1000 s^{-1} , a majority of the plastic strain can be attributed to have occurred through the slip-like propagation of a few dominant SBs (e.g., Figure 4h). Plasticity occurring via shear banding has dire consequences in amorphous metals/nanocrystalline metals: SBs are the typical cause of fracture under tensile loading and limit the amount of plastic strain that can be reached.^[39,42] During the plastic yielding of bulk metallic glass micropillars, propagation of SBs occurs typically by strain bursts, seen as distinct load drops, often leading to serrated stress-strain data.^[49,50] Micropillar compression studies on a-SiO₂ also show SB-mediated plasticity accompanied by serrated stress-strain behavior, indicating that the plasticity can be dominated by sudden pulses of plastic strain along the propagating SBs.^[22] To exclude the presence of possible load serrations in a-Al₂O₃, we performed supplementary nanoindentation with a Berkovich tip on $10 \mu\text{m}$ thick a-Al₂O₃ film. No load drops or serrations were observed, even though pyramidal tip indentation increases both the strain localization beneath the tip and the load applied (see Section S10, Supporting Information). We suggest that this is due to the up to 25-times higher bond switching activity at room temperature reported to occur in a-Al₂O₃ compared to a-SiO₂,^[12] leading also to the significantly enhanced activity of atoms exhibiting twice the average D^2_{min} (see Section S11, Supporting Information). This allows for a higher nucleation rate of LPSEs, and since we show that LPSEs ultimately also mediate the SB propagation, this results in a smoother and more gradual relaxation of stress without load serrations even during SB propagation-dominated plastic strain. In other words, we can state that the stress drops associated with the LPSE are

much lower than the load noise floor and load resolution of the nanoindenter in order to be detectable. The order of magnitude smaller activation volume of a-Al₂O₃ can also explain why individual load drops are significantly smaller and do not appear in the data (see Section S7, Supporting Information). Load drops in displacement-controlled indentation, or pop-ins in load-controlled indentation, have been routinely observed in metallic glasses and correlated with strain localization arising due to shear transformation zone activity. Serrations in the load-displacement behavior of metallic glasses typically decrease with increasing temperature, with mild or no serrations observed close to the glass transition temperature T_g ($T/T_g > 0.8$).^[51] In fact, metallic glasses have been shown to deform homogeneously at these high T/T_g temperatures even on macro-length scales.^[52] For comparison, the glass transition temperature T_g for a-Al₂O₃ is experimentally estimated to be 743 K .^[53] It remains to be studied whether the LPSEs occurring in oxide glasses have a similarity to the shear transformation zones attributed to mediate plasticity in bulk metallic glasses,^[50] and this should be addressed in future studies combining both material groups.

When brittle ceramics are tested with microcompression, a pillar typically fails by axial splitting, where the crack nucleates vertically from the pillar's top surface.^[18,19] This is likely due to tensile hoop stresses leading to tensile strains; this is caused by the pillar compression geometry as shown by the FEM modeling (Figure S5.2f, Supporting Information). In the case of a-Al₂O₃ micropillar compression, we did not detect the axial splitting phenomenon despite the presence of a similar tensile strain component. Instead, the propagating SBs intersected with the pillar surface and combined with the hoop stresses led to crack nucleation. At the highest measured strain rates, the cracks propagated up to a few hundreds of nanometers but again without fracture (Figure 4h, Figure 7b-c, and Figure S1.2, Supporting Information). As a difference to a-SiO₂,^[22] the data regarding the unloading phase also do not indicate any fracture. Visually the crack nucleation observed in a-Al₂O₃ is similar to the micropillars of single crystalline α -Al₂O₃, where the crack nucleates in the location where a dislocation slip intersects with the top surface of the pillar.^[20]

The FEM modeling allows us to replicate the experimental stress-strain behavior and qualitatively the shape of the a-Al₂O₃ pillar after compression (Figure 5). Rationalizing how the selected material "damage" model works, the material loses stiffness in the volume where the plastic deformation is first activated and that forces the plasticity to further concentrate on this softer volume. Based on experiments and atomistic simulations, the degree of lost stiffness appears to be related to the strain rate. At higher strain rates, we enforce a larger loss of stiffness, i.e., damage, leading to increasingly localized plasticity by SB propagation. We can deduce that the maximum damage remains lower at lower strain rates due to the relatively high activity of LPSEs in a-Al₂O₃, preventing the localization of plasticity. The successful matching of the FEM model with the experimental data can also give us valuable input in developing a theory predicting the plastic behavior of other amorphous oxides.

Several factors can induce spurious results regarding plasticity, either directly in the experimental or simulated mechanical data or in the following analysis of the data. Here we attempt to address all the outstanding issues. First, a high strain rate is known

to produce strong adiabatic heating, especially in high-strength materials.^[54] The adiabatic heating of the micropillar samples at higher strain rates could act to produce anomalous mechanical behavior, or for example, trigger the SB propagation. To study the potential effect of adiabatic heating, we determined the thermal diffusion distance of a-Al₂O₃ and compared that to the micropillar sample size (see Section S12, Supporting Information). The results show that even at the highest strain rate of 1000 s⁻¹ and for the largest specimens with the length of ≈20 μm, the thermal diffusion distance is 1–2 times larger than the sample. This means that all the performed mechanical tests are at most quasi-adiabatic, and sample heating did not significantly contribute to the experimental results if we assume that the plasticity is homogeneously distributed to the sample volume. It is possible that the localization of plasticity at higher strain rates induces “hot zones” inside the shear bands, and this could affect the measured stress-strain behavior or the observed plasticity. However, as all the samples deformed at the highest strain rate solely underwent plastic deformation and no fracture was observed, we leave the detailed study of this topic for the future.

Second, the presence of a strong enough electron beam can induce artificial plasticity in mechanical experiments.^[46,55] We performed dedicated experiments to study the effect that our SEM electron beam setup has on our micropillar samples during mechanical loading (see Section S13, Supporting Information). No significant difference was found in the mechanical behavior between the a-Al₂O₃ micropillar samples strained with electron beam On or Off. Therefore, the electron beam is not a source of plasticity in this study and does not contribute to the conclusions of this article.

Third, we selected the MD-simulated quenching method, box size, and strain rates to avoid inducing artificial ductility (see Section S14, Supporting Information).^[33]

Fourth, densification under compressive load is known to be able to induce plastic strain in a-SiO₂.^[32] To determine the role of densification in the plasticity of a-Al₂O₃, we measured the permanent change in density in a-Al₂O₃ under MD-simulated bulk compression and compared it to the behavior of a-SiO₂ under similar conditions (see Section S4, Supporting Information). The results show that densification of a-Al₂O₃ can contribute a maximum of ≈1.5% to the plastic strain along the axis under compressive stress, which, for example, at a maximum strain of 0.5 (50%) would translate to 0.0075 strain inflicted by densification. Therefore, densification has a negligible contribution to the plastic strain during the compression of a-Al₂O₃.

Fifth, small enough nanoscale samples exhibit decreased thermodynamic parameters, such as glass transition temperature.^[56] Parameters decreased close to or below room temperature could explain some features of the observed room temperature plasticity of a-Al₂O₃. However, the micropillars are large enough to insignificantly deviate from bulk thermodynamic properties. Recent experiments report a glass transition of 743 K for a-Al₂O₃.^[53] At room temperature, the flow of amorphous (experiments) and glassy (simulations) alumina occurs significantly below the reported glass transition temperature ($T/T_g = 0.4$), which is not explained by the current thermodynamic theory for oxide glasses.

Sixth, it is known that reducing the micropillar size can significantly change the mechanical properties of single crystalline metals.^[21] Our additional experiments with larger pillars

(Figure 7, Figure S9, Supporting Information) confirm that room temperature plasticity can be transferred to the bulk scale if the a-Al₂O₃ samples can be manufactured free of processing flaws.

4. Conclusions

Results from the a-Al₂O₃ micropillar compression experiments and simulations reveal exceptional microscale plasticity and clarify the design principles for damage-tolerant oxide glass materials. The experiments and simulations show that microscale a-Al₂O₃ samples can plastically deform without fracture at up to 50% strain. At the slowest strain rates (10⁻³ s⁻¹), the nucleation of localized plastic strain events produces a predominantly homogeneous plasticity that can fully accommodate the plastic strain. The nucleation rate of LPSEs was found to remain relatively constant at a constant temperature. To accommodate the required plastic strain at higher strain rates, the momentarily available LPSEs accumulate in Shear Bands (SBs), and their slip-like propagation takes over to account for an increasing portion of the measured plastic strain. At the highest strain rate (10³ s⁻¹), most of the plastic strain is mediated by a few dominant shear bands. Regardless, even at the highest experimental strain rate, the nucleation rate of LPSEs in a-Al₂O₃ is fast enough to avoid fracture. The microscale behavior of a-Al₂O₃ indicates that increasing the LPSE nucleation rate is a key property to obtain more damage-resistant oxide glass materials. Based on the current results and the earlier literature on a-Al₂O₃ and a-SiO₂, the LPSE nucleation rate is a material-specific property dictated by the atomic structure and can likely be found to be better or worse in other pure diatomic oxides. The results can be directly applied to design ultra-high strength and damage-tolerant micromechanical structures using a-Al₂O₃. In addition, if bulk amorphous oxides can be manufactured free of processing flaws, including required improvements in the manufacturing techniques, they show high potential to be used as light, high-strength, and damage-tolerant engineering materials.

5. Experimental Section

Film Deposition: All samples were processed by nanosecond UV laser (248 nm, Coherent GmbH, Germany) ablation of a polycrystalline Al₂O₃ target (Testbourne 99.99% purity) in a custom-made vacuum chamber (I-PLD300, Kenosistec s.r.l, Italy). The conditions used were: a laser repetition rate of 50 Hz; laser fluence of 3.5 J cm⁻²; background O₂ gas pressure of 0.15 Pa; target-substrate distance of 50 mm. The a-Al₂O₃ films were deposited on 30 mm x 50 mm silicon wafer substrates at room temperature with thicknesses up to 50 μm. The density of the PLD a-Al₂O₃ was estimated to be 3.47 ± 0.02 g cm⁻³.^[15] The films were measured to be amorphous using grazing incidence angle XRD and full amorphicity was further confirmed using a TEM cross-section of a deformed micropillar (see Figure S1.1, Supporting Information). For detailed characterization of microstructure and chemical composition of PLD a-Al₂O₃ samples, see Section S1, Supporting Information.

In Situ Micropillar Compression: Focused ion beam milling with a gallium source (Zeiss Crossbeam 540) was used to produce the micropillar samples from the 10 μm films deposited on a silicon wafer by PLD. Micropillar compression testing of PLD a-Al₂O₃ was performed in situ inside a Leo Zeiss SEM equipped with in situ SEM nanoindenter (Alemnis AG). All tests were carried out at room temperature. The temperature equilibrium between the instrument and sample was maintained by keeping the sample inside the system for an optimum duration of 2 h before testing. The average diameter (D) and height (h) of the pillars were measured to

be $\approx 2.25 \mu\text{m}$ and $4.5\text{--}5.0 \mu\text{m}$ respectively, resulting in an aspect ratio (h/d) of < 3 to avoid buckling of the specimen during experiments. As the pillars had an approximate taper angle of $2\text{--}3^\circ$, the pillar diameter required to determine the engineering stress was measured as the average diameter between the top and bottom diameters, and the average diameter of $2.25 \mu\text{m}$ was used to determine the engineering stress. Experiments were performed at different strain rates, varying from 10^{-3} s^{-1} to 10^3 s^{-1} , and individual pillars were tested only once. A diamond flat punch indenter tip (Synton MDP) of a diameter of $5 \mu\text{m}$ was used to compress the pillars. All tests were conducted in displacement-controlled mode to maintain a constant strain rate throughout each experiment. The tested pillars were imaged before and after the tests with FE-SEM (Zeiss Crossbeam 540) at an acceleration voltage of 1 kV . In addition, larger micropillars were tested with a diameter in the range of $6\text{--}11 \mu\text{m}$ and height in the range of $15\text{--}20 \mu\text{m}$, using a strain rate of 10^{-2} s^{-1} and a diamond flat punch with a diameter of $25 \mu\text{m}$. For these experiments, the micropillars were milled in a $\approx 50 \mu\text{m}$ thick PLD $\alpha\text{-Al}_2\text{O}_3$ film.

Atomistic Simulations: Large-scale molecular dynamics simulations with the LAMMPS software package were used to reveal atomic-scale phenomena active in $\alpha\text{-Al}_2\text{O}_3$ micropillar compression using the Matsui potential.^[57] Amorphous alumina was prepared using a melting-quenching process as mentioned by Gutiérrez et al.^[58] The bulk PBC setup (1) initial structure before straining was a rectangular cuboid with a size of $\text{ca. } 11 \times 11 \times 90 \text{ nm}^3$ including 963 300 atoms, and the corresponding structure was strained along the longest edge. The laterally unconfined setup (2) initial structure before straining is a cylinder with a size of $\approx 24 \text{ nm}$ in diameter and 50 nm in height including 2 082 480 atoms, and the structure was strained along the longest edge. Briefly, the system was first heated to 5000 K in an NVT ensemble for 45 ps at a density of 2.75 g cm^{-3} to erase the memory of the initial structure. Afterward, the structure was cooled down to 3000 K in 10 ps and equilibrated in the NVT ensemble at that temperature for 45 ps . The density was changed to 3.175 g cm^{-3} during equilibrium. Then, the system was cooled down to 300 K over 650 ps and 1 atmosphere . Finally, the system was relaxed for another 35 ps at 300 K . Periodic boundary conditions were applied to all dimensions for the bulk PBC structure, while in the laterally unconfined wire simulation, PBC was applied only along the z -axis. The compression simulations were performed by applying uniaxial compressive force on the structures prepared up to a maximum of 50% . Strain rates of $5.00 \times 10^7 \text{ s}^{-1}$, $5.00 \times 10^8 \text{ s}^{-1}$, and $5.00 \times 10^9 \text{ s}^{-1}$ were used in bulk PBC simulations, and a strain rate of $5.00 \times 10^8 \text{ s}^{-1}$ was used for the laterally unconfined nanopillar simulation. True stress was calculated using the momentary value of the cross-sectional area measured at each strain step, and engineering stress was calculated using only the initial cross-sectional area, which for the nanopillar simulation was approximated as a circle with a radius of 12 nm . Temperature was controlled with a thermostat (300 K , Nosé-Hoover method), and in the bulk PBC simulation, the NPT ensemble was applied in directions orthogonal to the compression using a barostat (1 atm , Nosé-Hoover method), leading to a plane stress-type of loading. The simulation box was deformed every timestep (1 fs) without remapping the atomic positions. Non-affine deformation D^2_{min} is the minimum value of the local atomic displacement and describes the local deviation from affine deformation compared to a reference configuration.^[38] Momentary D^2_{min} was calculated to characterize the nucleation of local plastic strain events (LPSEs) in amorphous alumina and a 1% interval of strain was used between the reference configuration and the configuration to be analyzed. The cut-off distance for the D^2_{min} calculation in alumina was 4.6 \AA .

Finite Element Simulations: In the framework of the continuum description of condensed matter, the commercial finite element analysis software Abaqus was utilized to model micropillar compression. Simulations were performed using a Static, General nonlinear geometry analysis step with automatic incrementation and a full Newton solution technique. The 3D simulation setup was developed as follows: The amorphous aluminum oxide ($\alpha\text{-Al}_2\text{O}_3$) micropillar is attached to the $\alpha\text{-Al}_2\text{O}_3$ substrate; the $\alpha\text{-Al}_2\text{O}_3$ substrate resides on the silicon wafer; and the diamond punch is placed on top of the micropillar. A surface-to-surface mechanical contact was defined between the interacting surfaces of the diamond punch and

the $\alpha\text{-Al}_2\text{O}_3$ micropillar. The model was meshed by 8-node linear brick finite elements with full integration (C3D8 element type). The diamond punch and silicon wafer were modeled as isotropic elastic materials. The $\alpha\text{-Al}_2\text{O}_3$ micropillar and substrate were modeled as isotropic elastic-plastic material with damage capabilities based on a damage model.^[40,41] The loading-unloading of the sample was simulated in two steps: During the first step, the diamond punch is moved toward the micropillar by applied displacement, and, during the second step, the diamond punch is moved back to its original position. For a more detailed description, see Section S5, Supporting Information.

Statistical Analysis: In data presented as “value \pm error”, the “value” is the mean calculated over the whole population, and “error” is estimated using the standard deviation method. Number of samples (n) used to draw each data plot in the figure is presented in the figure captions. log-log linear fitting was used to determine the slope for strain rate sensitivity m . Smoothing shown in Figure 3 and Figure 6 was done using an adjacent average method with 20 points of the window. Standard spreadsheet and Origin software were used to perform statistical analyses.

Supporting Information

Supporting Information is available from the Wiley Online Library or from the author.

Acknowledgements

The authors thank Annakaisa Frankberg for supporting the work. This work has received funding from the Academy of Finland (grant numbers 338750, 315451, 315452, 315453, 326426, 332347, 341050). The authors wish to acknowledge the CSC-IT Center for Science, Finland, for the generous computational resources (project no. 2003839 LAPLAS Glass Plasticity at Room Temperature). This work made use of Tampere Microscopy Center facilities at Tampere University and has received funding from the European Union's Horizon 2020 research and innovation program (grant agreement no. 841527).

Conflict of Interest

The authors declare no conflict of interest.

Author Contributions

A.L. and J.Z. contributed equally to this work. E.J.F. led the project and contributed to all the experiments and simulations, A.L. performed the micropillar compression experiments and contributed to the micropillar sample preparation, J.Z. performed the bulk MD simulations, J.K. performed the wire MD simulations, S.K. performed the FEM simulations, B.P. and M.C. deposited the $\alpha\text{-Al}_2\text{O}_3$ films, N.G.M. contributed to the micropillar sample preparation and characterization, T.S. contributed to the micropillar sample preparation, M.H. performed the adiabatic heating calculations, J.A. contributed to designing the molecular dynamics simulations, A.K. contributed to designing the molecular dynamic simulations, E.L. contributed to the design of the experiments, F.D.F. contributed to the design of the experiments, and G.M. contributed to the design of all the experiments. All authors contributed to the writing of the article. All data are available in the main article or in the supporting information. The authors would like to transparently point out that author F.D.F. has recently started a company that plans to commercialize products based on the material used herein.

Data Availability Statement

The data that support the findings of this study are available in the supplementary material of this article.

Keywords

finite element modelling, glasses, micropillar compression, molecular dynamics simulations, oxides, plasticity, pulsed laser deposition

Received: April 4, 2023

Revised: July 20, 2023

Published online:

- [1] A. A. Griffith, *Phil. Trans. R. Soc.* **1921**, A221, 163.
- [2] X. Yu, T. Marks, A. Facchetti, *Nat. Mater.* **2016**, *15*, 383.
- [3] K. Nomura, H. Ohta, A. Takagi, T. Kamiya, M. Hirano, H. Hosono, *Nature* **2004**, *432*, 488.
- [4] H. Hosono, J. Kim, Y. Toda, S. Watanabe, *Proc. Natl. Acad. Sci. USA* **2017**, *114*, 233.
- [5] G. Karbasian, M. S. McConnell, H. George, L. C. Schneider, M. J. Filmer, A. O. Orlov, A. N. Nazarov, G. L. Snider, *Appl. Sci.* **2017**, *7*, 246.
- [6] J. Y. Kim, S. H. Kim, H.-H. Lee, K. Lee, W. Ma, X. Gong, A. J. Heeger, *Adv. Mater.* **2016**, *18*, 572.
- [7] Y. Idota, T. Kubota, A. Matsufuji, Y. Maekawa, T. Miyasaka, *Science* **1997**, *276*, 1395.
- [8] A. Mavrič, M. Valant, C. Cui, Z. M. Wang, *J. Non-Cryst. Solids* **2019**, *521*, 119493.
- [9] T. T. Mattila, L. Vajavaara, J. Hokka, E. Husa, M. Mäkelä, V. Halkola, *Microelectron Reliab* **2014**, *54*, 601.
- [10] J. Agirrea, N. Otegia, D. Abedula, A. Orunaa, L. Galdosa, *Procedia Manuf* **2020**, *47*, 321.
- [11] K. Mahadevan, P. Liang, J. Fekete, *SAE trans.* **2000**, 109, 863.
- [12] E. J. Frankberg, J. Kalikka, F. G. Ferré, L. Joly-Pottuz, T. Salminen, J. Hintikka, M. Hokka, S. Koneti, T. Douillard, B. L. e Saint, P. Kreiml, M. J. Cordill, T. Epicier, D. Stauffer, M. Vanazzi, L. Roiban, J. Akola, F. Di Fonzo, E. Levänen, K. Masenelli-Varlot, *Science* **2019**, *366*, 864.
- [13] T. Du, H. Liu, L. Tang, S. S. Sørensen, M. Bauchy, M. M. Smedskjaer, *ACS Nano* **2021**, *15*, 17705.
- [14] Y. Zhang, H. Liu, S. Sundararaman, L. Huang, Y. Shi, *J. Am. Ceram. Soc.* **2022**, *105*, 958.
- [15] F. García Ferré, E. Bertarelli, A. Chiodoni, D. Carnelli, D. Gastaldi, P. Vena, M. G. Beghi, F. Di Fonzo, *Acta Mater.* **2013**, *61*, 2662.
- [16] F. Di Fonzo, D. Tonini, A. Li Bassi, C. S. Casari, M. G. Beghi, C. E. Bottani, D. Gastaldi, P. Vena, R. Contro, *Appl. Phys. A* **2008**, *93*, 765.
- [17] M. D. Uchic, D. M. Dimiduk, J. N. Florando, W. D. Nix, *Mater. Res. Soc. Symp. Proc.* **2002**, *753*, BB1.4.1.
- [18] P. R. Howie, S. Korte, W. J. Clegg, *J. Mater. Res.* **2011**, *27*, 141.
- [19] S. Korte-Kerzel, *MRS Commun.* **2017**, *7*, 109.
- [20] A. Montagne, S. Pathak, X. Maeder, J. Michler, *Ceram. Int.* **2014**, *40*, 2083.
- [21] M. D. Uchic, D. M. Dimiduk, J. N. Florando, W. D. Nix, *Science* **2004**, *305*, 986.
- [22] R. Ramachandramoorthy, J. Schwiedrzik, L. Petho, C. Guerra-Nuñez, D. Frey, J.-M. Breguet, J. Michler, *Nano Lett.* **2019**, *19*, 2350.
- [23] J. Hütsch, E. T. Lilleodden, *Scr. Mater.* **2014**, *77*, 49.
- [24] S. Korte, W. J. Clegg, *Philos. Mag.* **2011**, *91*, 1150.
- [25] J. J. Guo, K. M. Reddy, A. Hirata, T. Fujita, G. A. Gazonas, J. W. McCauley, M. W. Chen, *Acta Mater.* **2015**, *88*, 252.
- [26] E. Camposilvan, M. Anglada, *Acta Mater.* **2016**, *103*, 882.
- [27] M. Chen, J. Wehrs, A. S. Sologubenko, J. Rabier, J. Michler, J. M. Wheeler, *Mater. Des.* **2020**, *189*, 108506.
- [28] J. Michler, K. Wasmer, S. Meier, F. Östlund, *Appl. Phys. Lett.* **2007**, *90*, 043123.
- [29] M. Chen, J. Wehrs, J. Michler, J. M. Wheeler, *JOM* **2016**, *68*, 2761.
- [30] S. Korte, W. J. Clegg, *Scr. Mater.* **2009**, *60*, 807.
- [31] R. Lacroix, G. Kermouche, J. Teisseire, E. Barthel, *Acta Mater.* **2012**, *60*, 5555.
- [32] G. Kermouche, G. Guillonnet, J. Michler, J. Teisseire, E. Barthel, *Acta Mater.* **2016**, *114*, 146.
- [33] F. Yuan, L. Huang, *J. Non-Cryst. Solids* **2012**, *358*, 3481.
- [34] J. Luo, J. Wang, E. Bitzek, J. Y. Huang, H. Zheng, L. Tong, Q. Yang, J. Li, S. X. Mao, *Nano Lett.* **2016**, *16*, 105.
- [35] R. N. Widmer, A. M. Burnstead, M. Jain, T. D. Bennett, J. Michler, *J. Am. Chem. Soc.* **2021**, *143*, 20717.
- [36] T. To, S. S. Sørensen, M. Stepniewska, A. Qiao, L. R. Jensen, M. Bauchy, Y. Yue, M. M. Smedskjaer, *Nat. Commun.* **2020**, *11*, 2593.
- [37] M. Ballauff, J. M. Brader, S. U. Egelhaaf, M. Fuchs, J. Horbach, N. Koumakis, M. Krüger, M. Laurati, K. J. Mutch, G. Petekidis, M. Siebenbürger, T. Voigtmann, J. Zausch, *Phys. Rev. Lett.* **2013**, *110*, 215701.
- [38] M. L. Falk, J. S. Langer, *Phys. Rev.* **1998**, *E57*, 7192.
- [39] Z. F. Zhang, J. Eckert, L. Schultz, *Acta Mater.* **2003**, *51*, 1167.
- [40] Y. N. Rabotnov, Y. N., *Creep Problems in Structural Members*, North-Holland, Amsterdam **1969**.
- [41] L. M. Kachanov, *Introduction to Continuum Damage Mechanics*, Martinus Nijhoff, Dordrecht **1986**.
- [42] R. Narasimhan, P. Tandaiya, I. Singh, R. L. Narayan, U. Ramamurty, *Int. J. Fract.* **2015**, *191*, 53.
- [43] S. T. Liu, Z. Wang, H. L. Peng, H. B. Yu, W. H. Wang, *Scr. Mater.* **2012**, *67*, 9.
- [44] P. Kuppasami, V. S. Raghunathan, *Surf. Eng.* **2006**, *22*, 81.
- [45] J. Krim, *Surf. Sci.* **2002**, *500*, 741.
- [46] S. Bruns, C. Minnert, L. Pethö, J. Michler, K. Durst, *Adv. Sci.* **2023**, *10*, 2205237.
- [47] F. Yuan, L. Huang, *Sci. Rep.* **2014**, *4*, 5035.
- [48] A. Pedone, G. Malavasi, M. C. Menziani, U. Segre, A. N. Cormack, *Chem. Mater.* **2008**, *20*, 4356.
- [49] A. Dubach, R. Raghavan, J. F. Löffler, J. Michler, U. Ramamurty, *Scr. Mater.* **2009**, *60*, 567.
- [50] Z. Fan, Q. Li, C. Fan, H. Wang, X. Zhang, *J. Mater. Res.* **2019**, *34*, 1595.
- [51] C. A. Schuh, A. C. Lund, T. G. Nieh, *Acta Mater.* **2004**, *52*, 5879.
- [52] K. Zhao, X. X. Xia, H. Y. Bai, D. Q. Zhao, W. H. Wanga, *Appl. Phys. Lett.* **2011**, *98*, 141913.
- [53] H. Hashimoto, Y. Onodera, S. Tahara, S. Kohara, K. Yazawa, H. Segawa, M. Murakami, K. Ohara, *Sci. Rep.* **2022**, *12*, 516.
- [54] N. I. Vazquez-Fernandez, G. C. Soares, J. L. Smith, J. D. Seidt, M. Isakov, A. Gilat, V. T. Kuokkala, M. Hokka, *J. Dyn. Behav. Mater.* **2019**, *5*, 221.
- [55] K. Zheng, C. Wang, Y.-Q. Cheng, Y. Yue, X. Han, Z. Zhang, Z. Shan, S. X. Mao, M. Ye, Y. Yin, E. Ma, *Nat. Commun.* **2010**, *1*, 24.
- [56] J. H. Kim, J. Jang, W.-C. Zin, *Langmuir* **2001**, *17*, 2703.
- [57] M. Matsui, *Miner. Magn.* **1994**, *58A*, 571.
- [58] G. Gutiérrez, A. B. Belonoshko, R. Ahuja, B. Johansson, *Phys. Rev.* **2000**, *E61*, 9028.